Journal of the Physical Society of Japan **88**, 044705 (2019)
https://doi.org/10.7566/JPSJ.88.044705

# De Haas–van Alphen Experiment and Fermi Surface Properties in Field-Induced Ferromagnetic State of MnP

Shoya Kawakatsu[1], Masashi Kakihana[1], Miho Nakashima[2], Yasushi Amako[2], Ai Nakamura[3], Dai Aoki[3], Tetsuya Takeuchi[4], Hisatomo Harima[5], Masato Hedo[6], Takao Nakama[6], and Yoshichika Ōnuki[6]

[1]*Graduate School of Engineering and Science, University of the Ryukyus, Nishihara, Okinawa 903-0213, Japan*
[2]*Faculty of Science, Shinshu University, Matsumoto, Nagano 390-8621, Japan*
[3]*Institute for Materials Research, Tohoku University, Oarai, Ibaraki 311-1313, Japan*
[4]*Low Temperature Center, Osaka University, Toyonaka, Osaka 560-0043, Japan*
[5]*Graduate School of Science, Kobe University, Kobe 657-8501, Japan*
[6]*Faculty of Science, University of the Ryukyus, Nishihara, Okinawa 903-0213, Japan*

(Received November 28, 2018; accepted February 5, 2019; published online March 14, 2019)

MnP is a prototype 3*d*-itinerant magnet but still a compound under considerable study. This is based on the characteristic magnetic phases including the helical, cone, and fan structures and a variety of phase transitions with a Lifshitz tricritical point. The Fermi surface properties, however, have been scarcely studied. We have thus carried out a de Haas–van Alphen (dHvA) experiment using a high-quality single-crystal sample grown by the Sn-flux method. Many dHvA branches are observed, ranging from $2.8 \times 10^6$ to $9.45 \times 10^7$ Oe. The corresponding cyclotron effective masses are moderately heavy, $0.7 - 10m_0$ ($m_0$: rest mass of an electron), reflecting itinerant Mn-3*d* electrons.

## 1. Introduction

MnP with the orthorhombic (space group *Pnma*) structure is well known to exhibit several magnetic phases including the helical, cone, and fan structures and a variety of phase transitions with a Lifshitz point.[1–4] At zero magnetic field, it first becomes ferromagnetic at the Curie temperature $T_C = 292$ K, below which Mn spins are aligned parallel to the *b*-axis, changes the magnetic structure at $T^* = 282$ K, immediately below $T_C$, revealing that Mn spins are slightly tilted towards the *a*-axis, but on further cooling through $T_\alpha = 47$ K, a helical phase is formed. Note that the transition at $T^*$ has been observed recently and this new magnetic phase between $T^*$ and $T_\alpha$ exists only below a very small magnetic field of 5 Oe.[5–7] In the helical state, spins rotate in the helical *ab*-plane with the propagation vector $q = (0, 0, 0.117)$. Namely, the period is approximately nine lattice spacings along the *c*-axis. The ordered moment is $1.3\,\mu_B$/Mn.

Here, we note the crystal structure of MnP.[8] The space group belongs to *Pnma* ($a = 5.258$ Å, $b = 3.172$ Å, and $c = 5.918$ Å, $c > a > b$, No. 62), as shown in Fig. 1. This compound was, however, once reported on the basis of the space group of *Pbnm* ($a > b > c$, No. 62). The *a*-, *b*-, and *c*-axes in *Pnma* correspond to the *b*-, *c*-, and *a*-axes in *Pbnm*, respectively. In this paper, we follow the *Pnma* crystal structure, and the previous directions based on the *Pbnm* structure are shown in the brackets, for example, the *a*(*b*)-axis. A recent paper on the pressure-induced superconductivity of MnP employed the framework of *Pnma*.[9] It is characteristic that Mn atoms form a zigzag chain along the *a*(*b*)-axis, as shown in Fig. 1. Figure 1 is illustrated with eight unit cells, where the chemical unit cell contains four MnP molecules, which are named 1, 2, 3, and 4. It is characteristic that the same MnP-type compounds with the zigzag chain structure become superconductive, for example, in CrAs[10] and URhGe.[11]

A variety of phase transitions is characteristic in MnP, as shown in Fig. 2. The phase transitions at $T_C$ and $T^*$ are of second order, whereas the helical transition at $T_\alpha$ is of first order. Even in magnetic fields, the phase boundary at $T_\alpha$ is of first order. The $\lambda$-like line in the magnetic phase diagram, where three phases of the paramagnetic, ferromagnetic, and fan states are separated, exhibits an inflection point and the tricritical point is called the Lifshitz point, as shown in Figs. 2(a) and 2(c). The high-field magnetization indicates that the field-induced ferromagnetic (paramagnetic) states are realized in magnetic fields larger than 2.5 kOe for $H \parallel b(c)$-axis, 36 kOe for $H \parallel a(b)$, and 88 kOe for $H \parallel c(a)$.

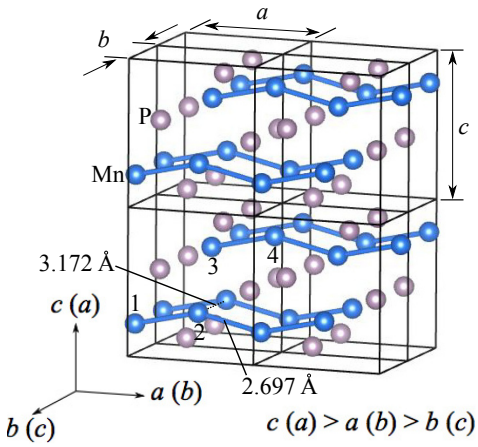


**Fig. 1.** (Color online) Orthorhombic crystal structure of MnP, which is based on *Pnma*. The directions of the *a*-, *b*-, and *c*-axes in *Pnma* were once presented as the *b*-, *c*-, and *a*-axes based on *Pbnm*, respectively, which are shown in brackets. Eight unit cells are shown, revealing a zigzag chain of Mn atoms along the *a*(*b*)-axis.

MnP was once grown by the Bridgman method. Namely, powders of Mn and P, which are encapsulated in a quartz tube, are gradually heated to 800 °C and then a powder of MnP is obtained. This powder is crushed into a fine powder and pressed into pellets. The pellets are inserted into an alumina crucible, encapsulated in a quartz tube, heated to 1170 °C, and slowly cooled in a temperature-gradient vertical electric furnace. Note that the melting point of MnP is $T_m = 1147$ °C. A single-crystal ingot with a large size of $10^\phi \times$

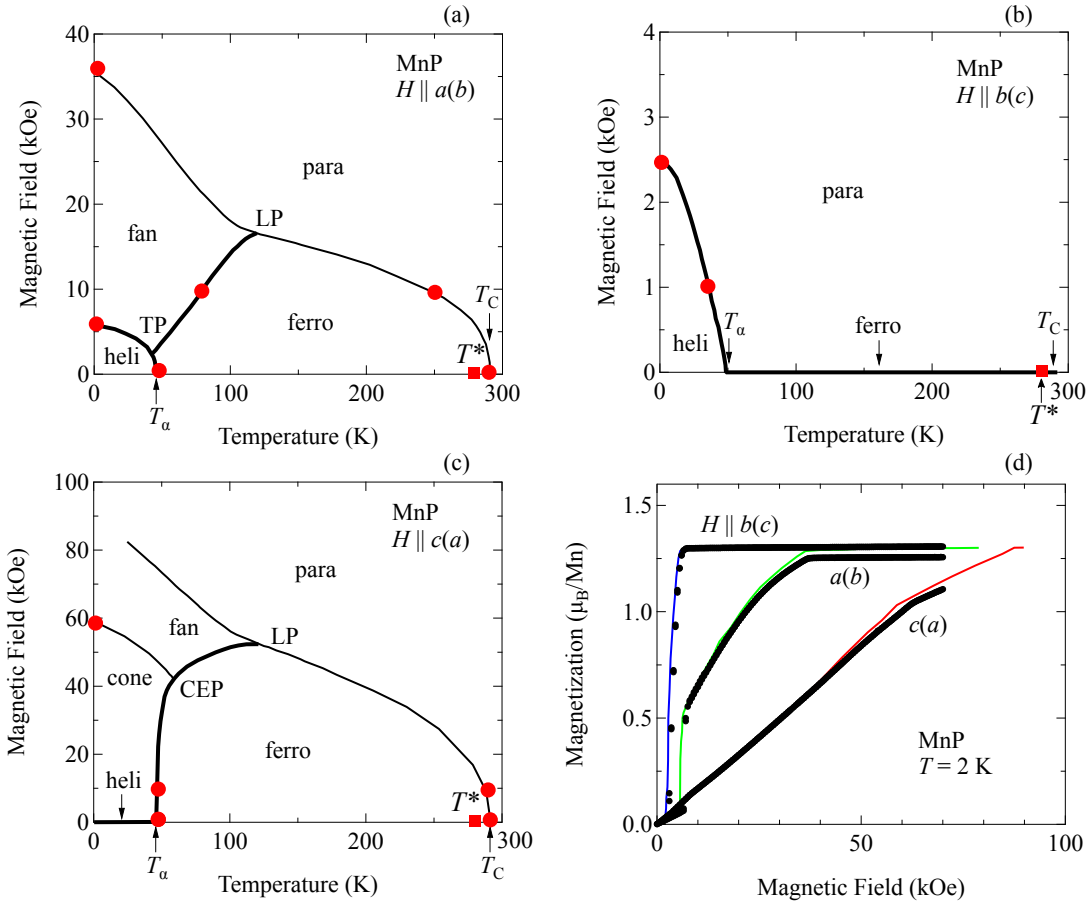


**Fig. 2.** (Color online) (a)–(c) Magnetic phase diagrams of MnP, cited from Ref. 5 and (d) magnetization curves at 4.2 K, cited from Ref. 3. $T^*$ values shown by solid squares are cited from Ref. 5. The present data are shown by solid circles.

50 mm$^3$ was obtained. The residual resistivity ratio RRR ($= \rho_{RT}/\rho_0$, $\rho_{RT}$: resistivity at room temperature, $\rho_0$: residual resistivity) was less than 100. Single crystals were also grown by the chemical transport method without a transport agent. Namely, MnP powder is set in a hotter part of the quartz tube at 850 °C and single crystals with 1 mm$^3$ are grown in a lower-temperature part at 800 °C. The RRR value was greatly improved, reaching 1300, and then the de Haas–van Alphen (dHvA) signals were observed using this sample.[12] Very recently, a simple Sn-flux method has been applied to MnP, where powders of Mn and P, together with Sn, with a constitution of Mn : P : Sn = 1 : 1 : 10, were inserted in an alumina crucible, encapsulated in a quartz tube, heated to 1150 °C, and cooled slowly, taking 10 days in total. The RRR value was 800–1100. High-quality single crystals are grown by this method.[9] MnP has been recently clarified to become superconductive under pressure, as mentioned above.

The dHvA amplitude, which is proportional to $\exp[-\alpha(m_c^*/H)(T + T_D)]$, is closely related to the sample quality, where $\alpha = 2\pi^2 c k_B/e\hbar$. If the cyclotron effective mass $m_c^*$ is the rest mass of an electron $1m_0$, the detecting temperature is usually 1 K in the dHvA experiment. A much lower temperature of 0.01 K is needed for $m_c^* = 100m_0$, for example, in $CeRu_2Si_2$.[13] Even if the lower temperature is realized using a dilution refrigerator, the reduction of $\exp[-\alpha(m_c^*/H)T_D]$ is inevitable in the dHvA amplitude. Here, $T_D$ ($= \hbar/2\pi k_B\tau$) is the so-called Dingle temperature, which is inversely proportional to the scattering lifetime of the carriers $\tau$. Therefore, a sample with a large $\tau$ value is essential to observe the dHvA oscillations for the heavy-fermion compounds including the 3*d*-itinerant magnet of MnP.

The previous dHvA measurement was carried out only for $H \parallel b(c)$ and $a(c)$ below 100 kOe.[12] The saturation field $H_c$ reaching 1.3 $\mu_B$/Mn is highly anisotropic with respect to the field direction, as mentioned above. Therefore, in the present paper, we carried out the dHvA experiment in magnetic fields larger than 80 kOe to clarify the Fermi surface properties in the field-induced ferromagnetic (paramagnetic) state using high-quality single crystals grown by the Sn-flux method.

## 2. Experimental Procedure

We grew single crystals by the Sn- and In-flux method. The starting materials were 4N(99.99% pure)-Mn, 4N-P, and 5N-Sn(and In) with a composition of Mn : P : Sn(In) = 1 : 1 : 10. The procedure of the single-crystal growth is the same as that described in Sect. 1. The insets of Fig. 3 show as-grown single crystals. One single crystal is elongated along the $a(b)$-axis, and the other is elongated along the $b(c)$-axis, with a typical size of $0.4 \times 3.5 \times 0.7$ mm$^3$. These single crystals are sufficient in size for the dHvA experiment.

The two kinds of single crystals mentioned above are typical of MnP. The crystal structure of MnP is based on a distortion of the hexagonal NiAs-type.[14,15] The displacement of Mn from the position of the NiAs structure is in the $c$–$a(b)$-plane, by 0.005 $c(a)$ along the $c(a)$-axis and 0.005 $a(b)$ along the $a(b)$-axis. The $a(b)$-axis corresponds to the hexagonal axis of the NiAs structure. The Mn atoms form zigzag chains along the $a(b)$-axis in MnP. The distance

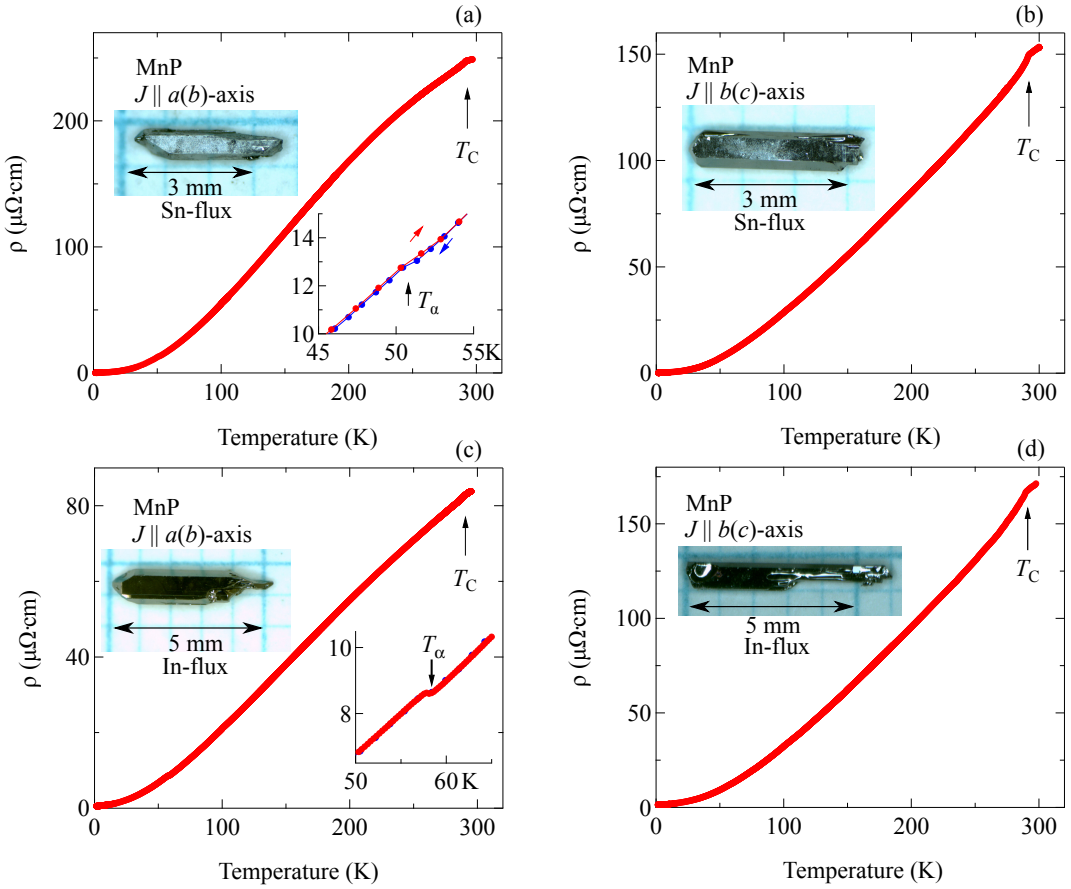


**Fig. 3.** (Color online) Temperature dependences of electrical resistivities in the current along the (a) *a*-axis and (b) *b*-axis of MnP. Single-crystal ingots of MnP grown by the Sn-flux method are shown in the insets. Similarly, the electrical resistivities in the current along the (c) *a*-axis and (d) *b*-axis of MnP grown by the In-flux method are shown with single crystals.

between two Mn atoms forming the zigzag chain is shortest, 2.697 Å. The Mn atoms are arranged in a straight line along the $b(c)$-axis, where the distance between two Mn atoms along the $b(c)$-axis is also short, 3.172 Å. These zigzag $a$–$b$($b$–$c$) planes are stacked along the $c(b)$-axis in MnP. Note that the lattice parameter of the $c(b)$-axis is largest, 5.918 Å. These might be the reasons why the two kinds of as-grown single crystals where elongated along the $a(b)$- and $b(c)$-axes.

The electrical resistivity was measured by the conventional four-terminal DC method. The magnetic susceptibility and magnetization were measured using a commercial superconducting quantum interference device (SQUID) magnetometer. The dHvA experiment was carried out by the standard field modulation method at a modulation frequency of 68 Hz and a modulation field of 100 Oe in strong magnetic fields up to 150 kOe.

## 3. Experimental Results and Analyses

First, we measured the electrical resistivity for the two kinds of single crystals elongated along the $a(b)$- and $b(c)$-axes, as shown in Fig. 3. For example, the resistivity for the $J \parallel a(b)$-axis, where the current flows in the direction of the elongated sample, has a kink at the Curie temperature $T_C = 291$ K and decreases monotonically with decreasing temperature. The inset shows a faint anomaly at $T_\alpha = 51$ K. The magnetic phase transition at $T^* = 282$ K is not found in the present measurement. The residual resistivity $\rho_0$ is $\rho_0 = 0.21$ μΩ·cm and the residual resistivity ratio is RRR = 1200, indicating a high-quality sample grown by the Sn-flux method, as shown in Fig. 3(a). Another sample grown by the Sn-flux method exhibits $\rho_0 = 0.26$ μΩ·cm and RRR = 580 for the $J \parallel b(c)$-axis, as shown in Fig. 3(b).

Similarly, samples grown by the In-flux method had values of $\rho_0 = 0.72$ μΩ·cm and RRR = 115 for the $J \parallel a(b)$-axis and $\rho_0 = 1.43$ μΩ·cm and RRR = 113 for the $J \parallel b(c)$-axis, as shown in Figs. 3(c) and 3(d), respectively. We used the present two single crystals grown by the Sn-flux method in the dHvA experiment.

Next, we measured the magnetization to confirm the highly anisotropic magnetic phase diagram. Figures 4(a)–4(c) show the temperature dependences of magnetizations under 1 and 10 kOe for $H \parallel a(b)$, $b(c)$, and $c(a)$, respectively. The magnetization curves at 2 K for $H \parallel a(b)$, $b(c)$, and $c(a)$ are also shown in Fig. 2(d) by solid circles in magnetic fields up to 70 kOe, where the data at 4.2 K, shown by solid lines, are cited from Ref. 3. The phase transitions shown by arrows in Figs. 4(a)–4(c) are shown in Figs. 2(a)–2(c), respectively, by solid circles in the magnetic phase diagrams.

The magnetic field corresponding to the saturation of the magnetization curves is thus highly anisotropic with respect to the field direction. We have simply carried out the dHvA experiment for magnetic fields larger than the saturation field in the magnetization, namely, above 80 kOe. We show in Figs. 5(a)–5(c) the dHvA oscillations for $H \parallel a(b)$, 48.5° tilted from the $a(b)$ to $b(c)$-axis, and the $b(c)$-axis, respectively, and the corresponding fast Fourier transforma-

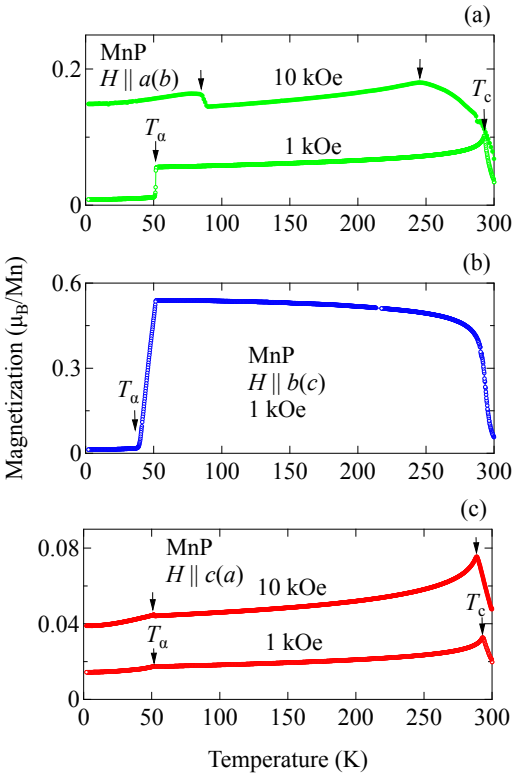


**Fig. 4.** (Color online) Temperature dependences of magnetizations under 1 and 10 kOe in MnP.

tion (FFT) spectra. The dHvA frequency $F$ ($= c\hbar S_F/2\pi e$), which was obtained from the FFT spectra of the oscillations, is proportional to the extremal (maximum and minimum) cross-sectional area $S_F$ of the Fermi surface, which is expressed as a unit of magnetic field. In these FFT spectra, the cyclotron effective masses $m_c^*$, which were obtained from the temperature dependences of the dHvA amplitudes, are presented. Many dHvA branches are observed, ranging from $2.8 \times 10^6$ to $9.45 \times 10^7$ Oe. The corresponding cyclotron masses are moderately heavy, ranging from 0.7 to $10m_0$ ($m_0$: rest mass of an electron).

The electronic specific heat coefficients $\gamma$ for conduction electrons are estimated to be as follows from the specific heat measurement in magnetic fields:[16] $9.65 \pm 0.5$ mJ/(K$^2$·mol) under 6 kOe for $H \parallel b(c)$, namely, in the field-induced ferromagnetic state, 6.9–9.1 mJ/(K$^2$·mol) under 10 kOe for $H \parallel a(b)$, namely, in the fan structure, and 5.4–7.6 mJ/(K$^2$·mol) in the helical structure ($H = 0$). These results indicate that Mn-3$d$ electrons produce a magnetic moment of 1.3 $\mu_B$ at each Mn site, together with the contribution to the 3$d$-itinerant conduction electrons with moderately large $\gamma$ values. The dHvA frequencies and cyclotron masses are summarized in Table I.

The sample was rotated against the magnetic field. Figure 6(a) shows the angular dependences of the dHvA frequencies in the field-induced ferromagnetic phase.

We carried out energy band calculations using a full-potential linearized augmented plane wave (FLAPW) method within the local spin density approximation (LSDA), where the field-induced ferromagnetic state was assumed and calculations were performed self-consistently. The spin–orbit coupling was simply neglected. The valence electrons were

**Table I.** Experimental dHvA frequencies and corresponding cyclotron effective masses, together with the theoretical dHvA frequencies and band masses in the field-induced ferromagnetic state of MnP.

| Experiment | | Theory | | |
|---|---|---|---|---|
| $F$ ($\times 10^7$ Oe) | $m_c^*$ ($m_0$) | branch | $F_b$ ($\times 10^7$ Oe) | $m_b$ ($m_0$) |
| MnP $H \parallel a(b)$-axis | | | | |
| 3.72 | 8.9 | $d_1$ | 6.60 | 1.34 |
| 3.38 | 1.4 | $a_1$ | 1.26 | 1.32 |
| 2.66 | 4.3 | $c_1$ | 0.39 | 0.55 |
| 1.81 | 4.8 | | | |
| 1.22 | 3.7 | | | |
| 1.00 | 3.6 | | | |
| 0.78 | 2.3 | | | |
| 0.47 | 0.7 | | | |
| 0.28 | 2.2 | | | |
| $H \parallel b(c)$-axis | | | | |
| 3.85 | 5.5 | $a_2$ | 3.63 | 2.06 |
| 3.63 | 4.3 | $b_2$ | 3.62 | 2.08 |
| 1.91 | 2.9 | $d_2$ | 1.73 | 0.39 |
| 1.53 | 2.1 | $c_2$ | 0.53 | 0.65 |
| 1.28 | 6.1 | | | |
| 1.09 | 4.4 | | | |
| 0.44 | 2.9 | | | |
| $H \parallel c(a)$-axis | | | | |
| | | $b_3'$ | 7.39 | 6.62 |
| | | $b_3$ | 5.52 | 5.05 |
| | | $a_3$ | 5.52 | 5.05 |
| | | $d_3$ | 5.62 | 1.88 |
| | | $c_3$ | 0.55 | 0.66 |
| $H \parallel \theta = 48.5°$ $a(b)$ to $b(c)$ | | | | |
| 9.45 | 9.1 | | | |
| 9.32 | 10.0 | | | |
| 4.03 | 9.8 | | | |
| 2.10 | 5.4 | | | |
| 1.31 | 5.0 | | | |
| 1.00 | 2.7 | | | |
| 0.50 | 2.5 | | | |
| 0.31 | 2.9 | | | |

$3p^6 3d^5 4s^2$ for the Mn atom and $3s^2 3p^3$ for the P atom. The lattice parameters were adopted from Ref. 8. The theoretical angular dependences of the dHvA frequencies and Fermi surfaces in the ferromagnetic state of MnP are shown in Figs. 6(b) and 6(c), respectively.

The energy band, and partial and total densities of states are shown in Fig. 7. The Fermi surfaces or conduction electrons are mainly due to Mn-3$d$ electrons. The Fermi surfaces consist of the bands 33 and 34 spin-down holes, 35 spin-down electron, and 39 and 40 spin-up holes, as shown in Figs. 6 and 7. From the self-consistent calculations, Mn-3$d$ electrons produce a magnetic moment of 1.3 $\mu_B$/Mn. The theoretical electronic specific heat coefficient $\gamma_b$ is 3.45 mJ/(K$^2$·mol). The experimental $\gamma$ value is moderately large, about 10 mJ/(K$^2$·mol), as mentioned above.

The present results of band calculations are almost the same as those in the previous and recent spin-polarized band calculations.[17–19] The band 33 spin-down (minority) hole and 34 spin-down (minority) hole surfaces are cylindrical along the $c^*$-axis but are connected to each other. On the other hand, two flat platelike Fermi surfaces are connected by a large arm, which correspond to the band 39 spin-up (majority) hole Fermi surface. The band 40 spin-up (majority) hole Fermi surface is just a platelike Fermi surface. The present platelike

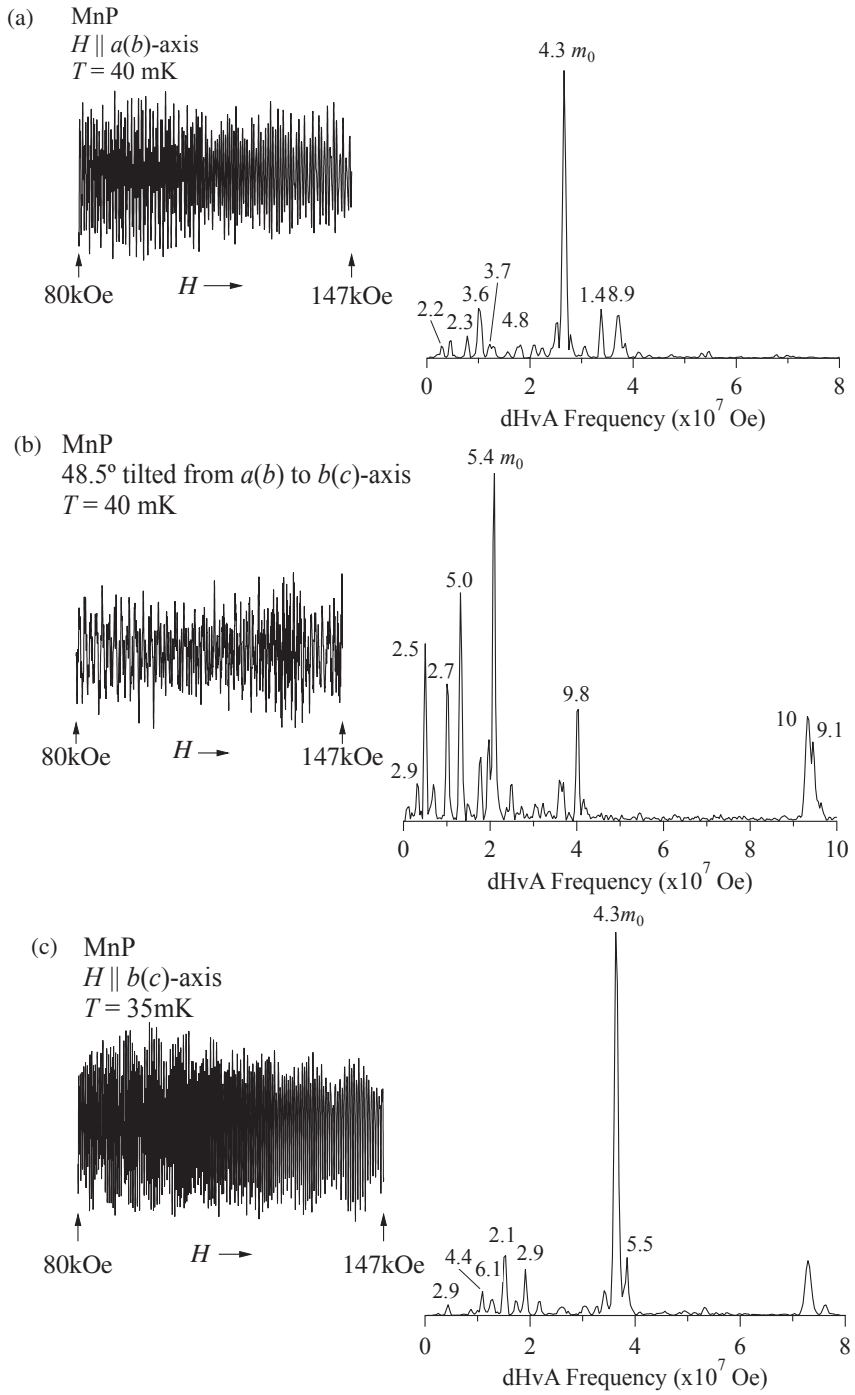


**Fig. 5.** Typical dHvA oscillations and corresponding FFT spectra in MnP, where figures in the FFT spectra represent the cyclotron effective mass $m_c^*$, revealing values of 2.1 to $10m_0$.

Fermi surfaces are illustrated clearly in Fig. 6(c)′ (electron version), where electrons are occupied in the Brillouin zone. The present one-dimensional-like Fermi surfaces are explained in recent papers,[18,19] where the Mn-3*d* orbital extends along the short and straight Mn chain along the *b*(*c*)-axis.

The present theoretical angular dependences of dHvA frequencies are not consistent with the experimental ones. The dHvA branches are not explained by the theoretical ones. This is not due to a lack of the spin–orbit interaction mentioned above. This is because we have recently clarified the Fermi surface properties of the antiferromagnet FeSn with the hexagonal structure.[20] The spin–orbit interaction is not included in the band calculations for FeSn. The reason for the present inconsistent result is unclear at present, but is most likely due to the crystal structure, where MnP crystallizes in the low-symmetric orthorhombic structure. This is left to a future study.

## 4. Summary

We grew high-quality single crystals of MnP with the orthorhombic crystal structure and carried out a dHvA experiment in the field-induced ferromagnetic state. Experimental results are summarized as follows:

(1) Two kinds of elongated single crystals were grown by the Sn-flux method, where the elongated directions are along the *a*(*b*)- and *b*(*c*)-axes.

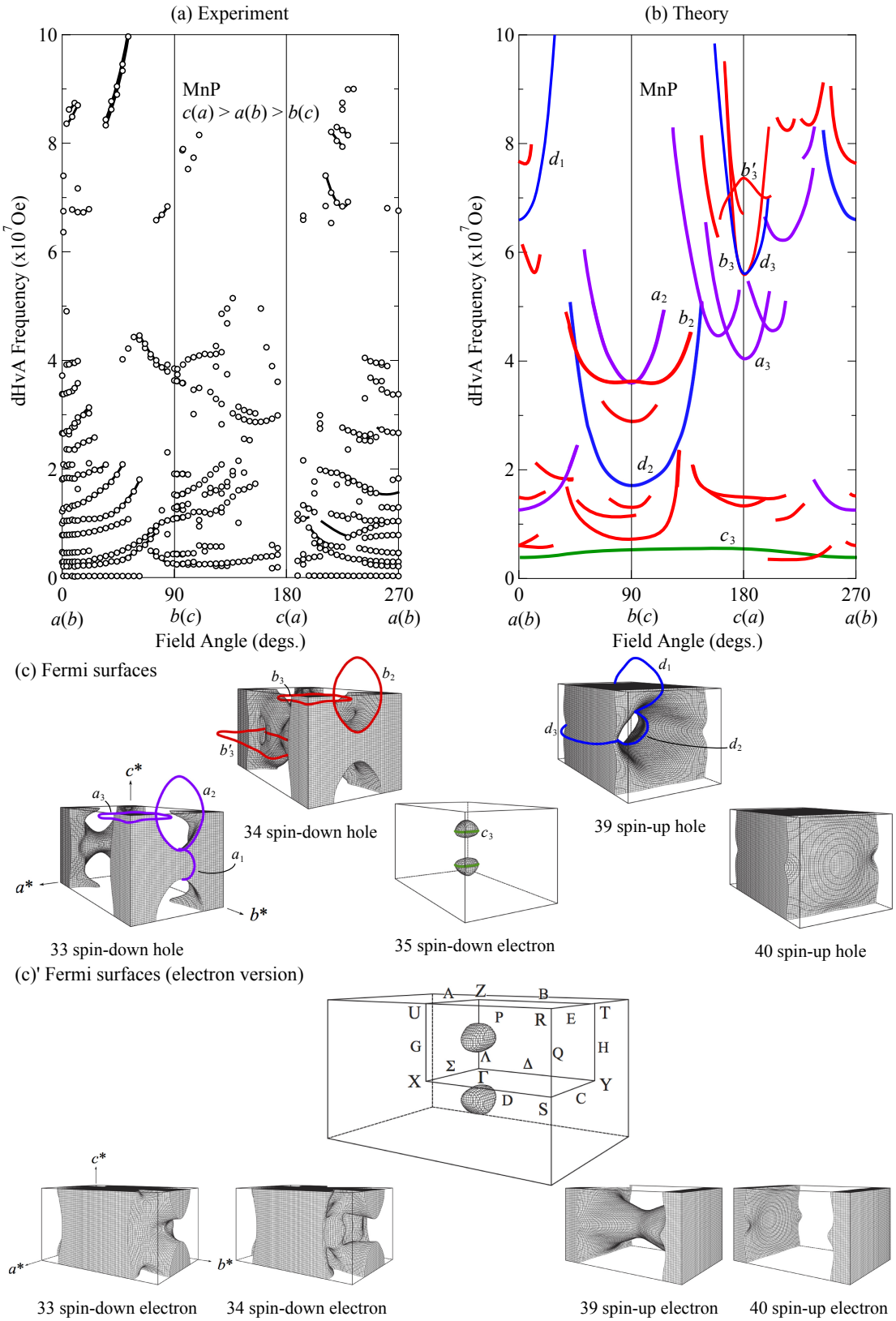


**Fig. 6.** (Color online) (a) Angular dependences of dHvA frequencies, (b) corresponding theoretical dependences in the ferromagnetic state of MnP, and (c) theoretical Fermi surfaces, together with (c)′ the theoretical Fermi surfaces occupied by electrons.

(2) The present sample is of extremely high quality, with $\rho_0 = 0.21\,\mu\Omega\cdot$cm and RRR = 1200 for the current along the $a(b)$-axis.
(3) Many dHvA branches are detected in the range from $F = 2.8 \times 10^6$ to $9.45 \times 10^7$ Oe. The dHvA branches are multiply connected, and simple closed Fermi surfaces are not detected in MnP.
(4) The cyclotron effective masses are moderately large, ranging from 0.7 to $10m_0$. The Fermi surfaces are mainly composed of Mn-3$d$ electrons.

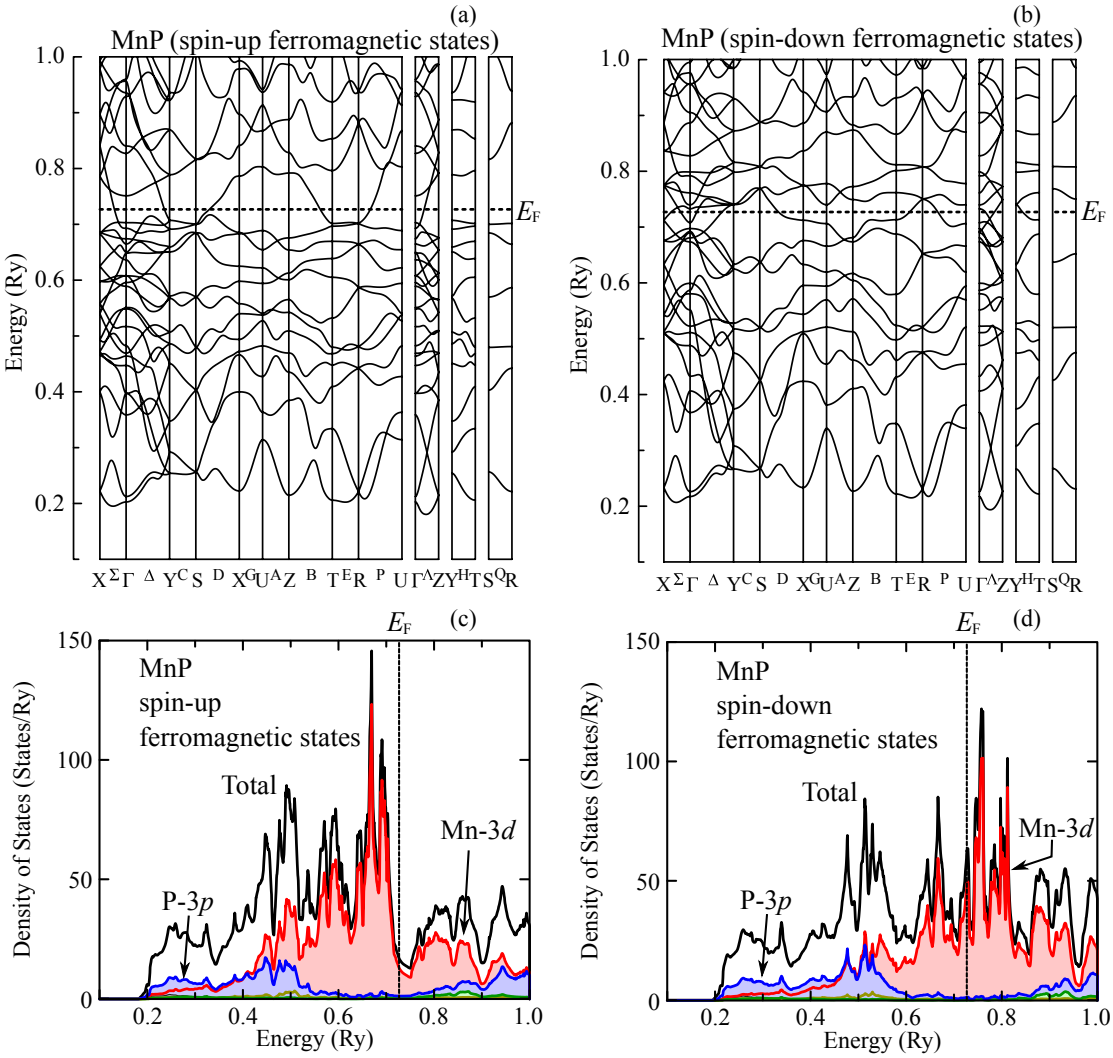


**Fig. 7.** (Color online) (a) and (b) Energy bands in the spin-up and spin-down ferromagnetic states, and (c) and (d) corresponding partial and total densities of states in the ferromagnetic state of MnP, respectively.

(5) The detected dHvA branches are, however, not explained by the full-potential linearized augmented plane wave method within the local spin density approximation. The reason is unclear, but is most likely due to the low-symmetric orthorhombic structure of MnP, which is left to a future study.

**Acknowledgments** We are grateful to Professor Massimo Nespolo for his helpful advice on the crystal structure of MnP. This work was supported by JSPS KAKENHI Grant Nos. JP18H043298, JP17K05547, JP16K05453, JP15H05884, JP15H05882, and JP15H05886, and Grant-in-Aid for JSPS Research Fellow No. JP18J15180.

1) A. Ishizaki, T. Komatsubara, and E. Hirahara, Prog. Theor. Phys. Suppl. **46**, 256 (1970).
2) C. C. Becerra, Y. Shapira, N. F. Oliveira, and T. S. Chang, Phys. Rev. Lett. **44**, 1692 (1980).
3) Y. Shapira, N. F. Oliveira, C. C. Becerra, and S. Foner, Phys. Rev. B **29**, 361 (1984).
4) A. Zięba, C. C. Becerra, H. Fjellvåg, N. F. Oliveira, Jr., and A. Kjekshus, Phys. Rev. B **46**, 3380 (1992).
5) C. C. Becerra, J. Phys.: Condens. Matter **12**, 5889 (2000).
6) T. Yamazaki, Y. Tabata, T. Waki, H. Nakamura, M. Matsuura, and N. Aso, J. Phys.: Conf. Ser. **200**, 032079 (2010).
7) T. Yamazaki, Y. Tabata, T. Waki, T. J. Sato, M. Matsuura, K. Ohoyama, M. Yokoyama, and H. Nakamura, J. Phys. Soc. Jpn. **83**, 054711 (2014).
8) S. Rundqvist and P. C. Nawapong, Acta Chem. Scand. **19**, 1006 (1965).
9) J.-G. Cheng, K. Matsubayashi, W. Wu, J. P. Sun, F. K. Lin, J. L. Luo, and Y. Uwatoko, Phys. Rev. Lett. **114**, 117001 (2015).
10) H. Kotegawa, S. Nakahara, H. Tou, and H. Sugawara, J. Phys. Soc. Jpn. **83**, 093702 (2014).
11) D. Aoki, A. Huxley, E. Ressouche, D. Braithwaite, J. Flouquet, J.-P. Brison, E. Lhotel, and C. Paulsen, Nature **413**, 613 (2001).
12) M. Ohbayashi, T. Komatsubara, and E. Hirahara, J. Phys. Soc. Jpn. **40**, 1088 (1976).
13) Y. Ōnuki and R. Settai, Low Temp. Phys. **38**, 89 (2012).
14) T. Suzuki, J. Phys. Soc. Jpn. **25**, 1548 (1968).
15) W. Tremel, R. Hoffmann, and J. Silvestre, J. Am. Chem. Soc. **108**, 5174 (1986).
16) A. Takase, H. Yashima, and T. Kasuya, J. Phys. Soc. Jpn. **47**, 531 (1979).
17) A. Yanase and A. Hasegawa, J. Phys. C **13**, 1989 (1980).
18) Y. Xu, M. Liu, P. Zheng, X. Chen, J. G. Cheng, J. Luo, W. Xie, and Y. F. Yang, J. Phys.: Condens. Matter **29**, 244001 (2017).
19) P. Zheng, Y. J. Xu, W. Wu, G. Xu, J. L. Lv, F. K. Lin, P. Wang, Y. F. Yang, and J. L. Luo, Sci. Rep. **7**, 14178 (2017).
20) M. Kakihana, K. Nishimura, D. Aoki, A. Nakamura, M. Nakashima, Y. Amako, T. Takeuchi, T. Kida, T. Tahara, M. Hagiwara, H. Harima, M. Hedo, T. Nakama, and Y. Ōnuki, J. Phys. Soc. Jpn. **88**, 014705 (2019).